Sensing and tuning microfiber chirality with nematic chirogyral effect

Simon Čopar, David Seč, Luis E. Aguirre, Pedro L. Almeida, Mallory Dazza, Miha Ravnik, Maria H. Godinho, Pawel Pieranski, and Slobodan Žumer

Phys. Rev. E **93**, 032703 — Published 15 March 2016

DOI: 10.1103/PhysRevE.93.032703

Sensing and tuning microfiber chirality with nematic chirogyral effect

Simon Čopar,[1] David Seč,[1] Luis E. Aguirre,[2] Pedro L. Almeida,[2,3] Mallory Dazza,[4,5] Miha Ravnik,[1,6] Maria H. Godinho,[2] Pawel Pieranski,[4] and Slobodan Žumer[1,6]

[1] *Faculty of Mathematics and Physics, University of Ljubljana, Jadranska 19, 1000 Ljubljana, Slovenia*
[2] *CENIMAT/I3N, Departamento de Ciência dos Materiais, Faculdade de Ciências e Tecnologia, FCT, Universidade Nova de Lisboa, Campus da Caparica, 2829-516 Caparica, Portugal*
[3] *Área Departamental de Física, Instituto Superior de Engenharia de Lisboa, ISEL, Instituto Politécnico de Lisboa, R. Conselheiro Emídio Navarro, 1, 1959-007 Lisboa, Portugal*
[4] *Laboratoire de Physique des Solides, Université Paris-Sud, France*
[5] *École normale supérieure de Cachan, 61, avenue du Président Wilson, 94235 Cachan, France*
[6] *J. Stefan Institute, Jamova 39, 1000 Ljubljana, Slovenia*

Microfibers with their elongated shape and translation symmetry can act as important components in various soft materials, notably for their mechanics on the microscopic level. Here we demonstrate the mechanical response of a micro object to imposed chirality, in this case, the rotation of disclination rings in an achiral nematic medium caused by the chiral surface anchoring on an immersed microfiber. This coupling between chirality and mechanical response, used to demonstrate sensing of chirality of electrospun cellulose microfibers, is revealed in the optical micrographs due to anisotropy in the elastic response of the host medium. We provide an analytical explanation of the chirogyral effect supported with numerical simulations, and perform an experiment to test the effect of the cell confinement and fiber size. We controllably twist the microfibers and demonstrate the response of the nematic medium. More generally the demonstrated study provides means for experimental discrimination of surface properties, and allows mechanical control over the shape of disclination rings.

I. INTRODUCTION

Liquid crystalline fluids are interesting materials for various applications, where tunability, optical anisotropy and sensitivity to external fields and confinement are important. Sensitivity of liquid crystals to surface chemistry is already used today for biological and biochemical sensors [1, 2], including sensors for pathogens [3] and chemical agents [4, 5]. Rheological, optical and sensing features can be used in microfluidic circuits to create low cost lab-on-chip devices [6, 7].

Nematic colloids and emulsions with inclusions of different shapes and surface properties have been investigated experimentally and numerically [8–11]. Boundary conditions imposed by the inclusions in a nematic liquid crystalline (NLC) medium induce elastic deformations in the orientational order of molecules with topological defects, such as point defects (hedgehogs) and disclination loops that can be even linked or knotted [12, 13]. The tendency to minimize the distortion leads to defect-driven self-assembly. These systems have been studied as candidates of self-assembled and reconfigurable materials for use in optics [14], lasing [15], selective refraction [16], in microfluidics [17], or as memory materials [18] and metamaterials [19–21].

Elongated objects, including microrods [22, 23], introduce orientation-dependent behavior, multiple metastable states and possibility of assembly into clusters of various shapes. Microrod suspensions, self-assembled in a liquid crystalline host, are being studied as potential tunable metamaterials [24, 25].

The defect structures and their stability depend on the nature of coupling between the surface of the inclusion and nematic director that is constrained by the field determined by its surroundings. The homeotropic anchoring of long rod-like inclusions is analyzed in the reference [26]. The anchoring determined by preferred relative orientation of nematic molecules to the surface depends on the chemistry and anisotropic nanostructure of the surface, which was recently exploited to investigate properties of biological microfibers by depositing nematic microdroplets on the fibers [27]. Microfibers can be used as optical waveguides, which coupled with versatile assembly techniques build towards soft optical circuits [6, 28].

The listed studies stimulated us to focus this paper on effects of nontrivial nematic anchoring on fibers in a NLC constrained by a homogeneous far-field. We consider a nematic cell with homeotropic (perpendicular) anchoring as a probe of the surface properties of immersed cellulose acetate (CA), hydroxypropylcellulose (HPC) and nylon fibers. Cellulose fibers are produced by electrospinning – drawing of fibers from a liquid phase using strong electric field – and vary in thickness and surface anchoring. The planar surface anchoring of the nematic molecules on untreated fibers induces formation of domains of aligned director field, interspaced with topological defects in the form of disclination rings. We investigate the disclination rings and the director with polarized optical microscopy and deduce the director field structure around the fiber by observing the tilting of disclination rings in response to the helical planar anchoring on the fiber surface – the chirogyral effect. Further experiments with thicker fibers are demonstrated, where the helicity of the alignment of the fiber surface and confinement inside a cell are me-

chanically adjustable, revealing the coupling mechanism between surface induced microchirality and the surrounding soft complex fluid. We compare the experiments with numerical simulations and construct an analytical model of the director that describes the shape and orientation of the observed disclination rings, making a qualitative prediction of the chirogyral effect.

II. EXPERIMENTAL SETUP

Micron-scale cellulose fiber networks are produced by electrospinning and deposited between two aluminum electrodes (for more, see Ref. [29]). Hydroxypropylcellulose (HPC) (Aldrich, $M_w = 100\,000$ g /mol) and cellulose acetate (CA) (Aldrich, $M_w = 60\,000$ g /mol, 40% acetyl groups) filaments are electrospun from anisotropic and isotropic solutions, respectively. The HPC fiber diameters are in the range of $1 - 3$µm while the CA ones are in between $0.5 - 1.5$µm.

The NLC cells were prepared by overlapping two square glass substrates (15×15mm ^{2}). The inner surfaces were treated by spin coating with a solution of lecithin (from egg yolk – Sigma Aldrich) in acetone (12% w/w), to induce a homeotropic anchoring of the NLC. The acetone was allowed to evaporate at room temperature and then the substrates were kept at 50 °C for 30 minutes before use. The electrospun cellulose fibers were enclosed by the two treated glasses keeping the gap between them constant through the use of two flat spacers with a thickness of 12 µm for CA fibers and 15 µm for HPC fibers, ensuring that the fibers do not touch the boundaries. The cells were then filled with the NLC 4'-n-pentyl-4-cyanobiphenyl (5CB from Merck) by capillarity and sealed. The samples were observed by using a polarizing optical microscope (POM) Olympus BX51 coupled to a CCD DP73 camera, under parallel polarizers and between crossed polarizers with or without an optical retardation plate (a plate with a phase delay of one cycle at $\lambda = 530$ nm). The retardation plate (lambda-plate) breaks the mirror symmetry in the micrograph, which helps discriminate between clockwise and counterclockwise director deviations from polarizer/analizer direction [22]. Disclination rings were produced with temperature quenches. The sample's temperature was controlled by the use of a heating/cooling stage Mettler FP90.

To study the effect of fiber helicity quantitatively, a different experimental setup was used. A cell was assembled using two glass slides equipped with ITO electrodes treated with the polyimide SE-1211 from Nissan Chemical (received from P. Oswald) for the homeotropic anchoring. The slides were separated by 100 µm spacers (Meltonix 1170-100). This cell was filled with the nematic eutectic mixture EN18 (received from Heinz Kitzerow) and a drawn-by-hand HPC fiber was inserted into it. One end of the fiber was clamped while the other one was rotated around the fiber axis until a suitable torsion was obtained. In this setup, instead of a temperature quench, a 100 Hz AC voltage was applied to create the disclination rings.

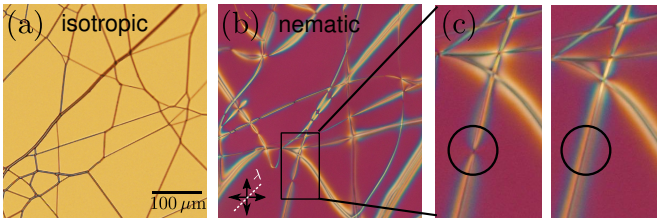

FIG. 1. (Color) (a,b) The micrograph of a network of cellulose microfibers in a nematogenic host in isotropic and nematic phase, respectively. In the nematic phase, the fibers are surrounded by colors that indicate different orientation of the director field in the imaging plane. (c) After each temperature quench, the long-lived nematic defects that are seen on the fibers, appear randomly at different positions. This confirms that the defects are not caused by imperfections on the fiber. Image (a) is taken between parallel polarizers while (b,c) are taken between crossed polarizers with an lambda-plate to create the color contrast.

The experiment with the twisted Nylon fiber was made using a third, more sophisticated setup. The Nylon fiber was rubbed to obtain planar anchoring along the length of the fiber, and attached on its two ends to axes of stepping motors allowing to twist the fiber as needed. The cell was made using two 12×25 mm glass slides equipped with ITO electrodes treated with the polyimide for the homeotropic anchoring. Experiments with lecithin coated glass slides have been performed as well without any noticeable difference in results. The cell was supported by a xyz translation stage; one slide was fixed while the other one was supported by a system equipped with three screws allowing to control the distance between the slides and their parallelism. At the beginning of experiments, the Nylon fiber was located outside of the cell which was filled with the NLC (EN18, MBBA or 5CB). Subsequently, a small droplet of the NLC was deposited on the fiber with the aim to generate one disclination ring in it [27, 30]. Finally, the fiber carrying a droplet with a solitary disclination ring was inserted into the cell.

III. OPTICAL OBSERVATION OF DISCLINATION RINGS

Deposition of electrospun cellulose fibers produces a network of fibers with varying thicknesses and orientations, as shown in Figure 1a,b. The network is immersed in 5CB in the isotropic phase and cooled across the transition into the nematic phase, which forces the molecular orientation – the director – to negotiate the boundary conditions on the surface of the fiber and the homeotropic alignment on the cell walls. Domains of different textures satisfying the boundary conditions appear, interspaced

by topological defects in the form of disclination rings that encircle the fiber. A homeotropic cell has no preferred orientation in the imaging plane, so the defects and the domain patterns follow the same rules, regardless of the orientation of the fiber.

Figure 1b,c shows that after every quench from isotropic to the nematic phase, the relaxation may take a different dynamic trajectory, creating visually discernible topological defects at different positions on each run. Close observation of such a defect (Fig. 1c) shows, that the polarization micrograph colors change between left and right side of the defect. The topological and elastic nature of these defects and the effect of the fiber surface to their in-plane orientation are explored in the following sections.

The cellulose pulled into fibers has the polymer chains aligned predominantly parallel to the fiber. The nematic anchoring on the surface of such a fiber follows this axial direction, as observed in previous experiments [31]. The surrounding bulk director field is such that on the top and the bottom side of the fiber, the director field has to curve from vertical (perpendicular to the top and bottom plates) to horizontal (along the fiber). This "escape" of the director from perpendicular to an axial alignment can happen in either direction along the fiber, and the resulting textures are mirror images of each other. If the escape direction alternates on different parts along the fiber, the resulting "domains" are interspaced by disclination rings (Fig. 2a). Each of these rings has a director profile that varies between typical planar cross sections with $\pm 1/2$ winding number at top and bottom parts, and a twisted profile on left and right parts of the fiber. They all carry zero topological charge, which is easily verified: a topological defect with charge q has each direction appearing at least $|q|$ times on any enclosing surface surrounding the defect. In our cell, the maximum deviation from the vertical orientation is around 90° just next to the fiber, so about half of the directions do not even appear once, thus proving that our topological structures are charge-neutral. This is in a fundamental contrast with the case of fibers with homeotropic (perpendicular) surface anchoring, where the disclination rings alternate between ± 1 topological charges [26]. The disclination rings and domains alternate in orientation, which is visible in the optical micrographs (Fig. 2b,c).

The details of the director field around the fibers depend on the elastic properties of the host nematic medium. In general, a nematic material can respond differently to the splay, twist and bend deformation modes, described by three Frank elastic constants [32]. Under a commonly adopted assumption, that all three elastic constants are equal, the director field would only vary in the vertical plane spanned by the fiber axis and the cell normal (yz plane in Fig. 2a). The projection of the long molecular axis to the imaging plane would be constant, so polarization of the transmitted light would not be rotated and the polarizing optical micrographs would show no discernible patterns. The observed color and contrast variation in the micrographs thus indicate on the importance of elastic anisotropy, i.e. multiple elastic constants.

To investigate the mechanism that produces the nematic profiles seen in experiments, we varied the elastic constants in our numerical simulations based on free-energy minimization of the Landau-de Gennes free energy. The bulk contribution to the free energy includes three elastic constants,

$$f = \frac{1}{2}AQ_{ij}Q_{ji} + \frac{1}{3}BQ_{ij}Q_{jk}Q_{ki} + \frac{1}{4}C(Q_{ij}Q_{ji})^2 + \quad (1)$$

$$\frac{1}{2}L_1(Q_{ij,k})^2 + \frac{1}{2}L_2(Q_{ij,j})^2 + \frac{1}{2}L_3Q_{ij}Q_{kl,i}Q_{kl,j}. \quad (2)$$

Tensorial elastic constants $L_{1,2,3}$ are related to Frank elastic constants $K_{1,2,3}$ via relations $L_1 = \frac{2}{27S^2}(-K_1 + 3K_2 + K_3)$, $L_2 = \frac{4}{9S^2}(K_1 - K_2)$ and $L_3 = \frac{4}{27S^3}(-K_1 + K_3)$ where K_1, K_2, K_3 are splay, twist and bend elastic constant, respectively, and S the nematic degree of order measured in the same conditions as the elastic constants [33]. We set $K_1 = K_3 = 50\,\mathrm{pN}$, which have been used in the past as a good compromise between computational feasibility and agreement with 5CB experiments [34, 35], and only varied the ratio K_1/K_2. We also assume that the unidirectional planar anchoring on the fiber is strong enough, so that the effect of saddle-splay elasticity can be safely ignored.

With equal elastic constants $K_1 = K_2 = K_3$, the simulated transmission micrograph is homogeneous, as expected (not depicted). Decreasing the twist elastic constant relative to the other two ($K_2 < K_1 = K_3$) results in increasingly significant colored fringes around the fiber, producing an image that qualitatively reproduces the experimental result (Fig. 2b,c). Recall that except for its effect on relative defect thickness, the overall scale of the elastic constants and system size plays only a minor role in the director field properties that produce the observed effect.

The difference in the elastic constants breaks the symmetry and prefers the director to also vary in the direction transverse to the fiber axis (Fig. 2d). Angles of deflection in the horizontal (xy) plane are typically less than 20°, but result in a clearly observable color contrast in the transmission micrograph, similar to the observation in Ref. [36]. The elastic anisotropy is therefore not merely a perturbation but an essential mechanism without which the observation of the director with this method would not be possible.

IV. THE CHIROGYRAL EFFECT

Disclination rings on the HPC fibers are not aligned perpendicular to the fiber, like rings on the CA fibers are, but are tilted (see the example in Fig. 3a,b), which indicates a different interaction between the fiber surface and the surrounding nematic. A similar effect was

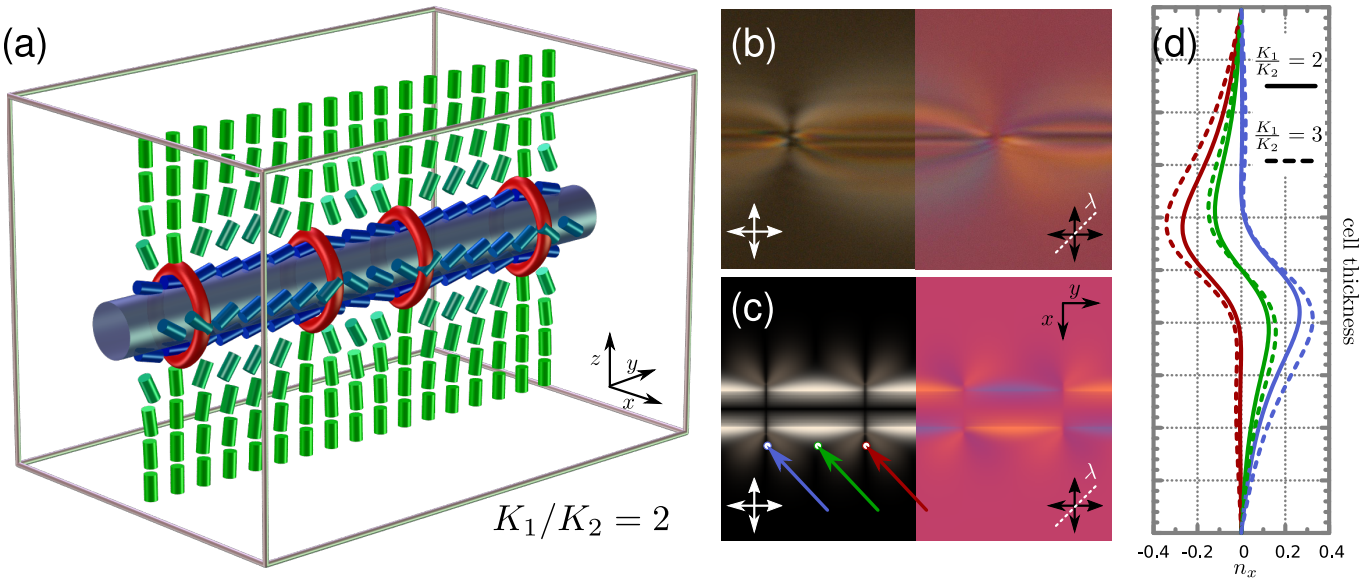

FIG. 2. (Color) (a) A simulated director field structure that shows how the molecular orientation rotates from vertical on the top/bottom plates to horizontal on the fiber. The direction of this "escape" alternates on domains interspaced by ring defects. (b) Experimental optical micrograph of CA fibers without (left) and with (right) lambda-plate (oriented at 45° with respect to the polarizers). The colors would not be seen if the in-plane component of the director, which causes birefringence, had been exclusively in the y direction. (c) Simulated reconstruction of the micrographs seen in panel (b) with twist elastic constant anisotropy $K_1/K_2 = 2$. A short segment of a fiber was simulated and shown. (d) Variation of the x component of the director along a vertical line at three locations in the cell, marked in panel (c) with the same colors. The deviation of the director towards x alternates between top and bottom at the rings, and is symmetric between the rings. Increasing elastic anisotropy also increases the deviation.

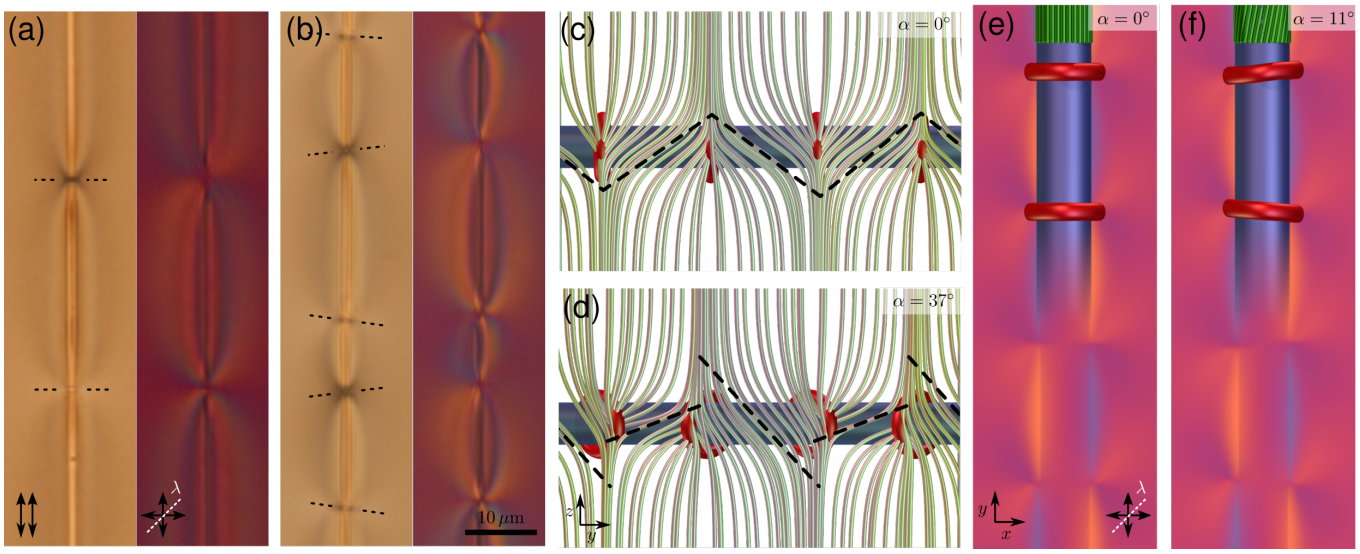

FIG. 3. (Color) (a,b) POM pictures of CA (a) and HPC (b) fibers observed between parallel polarizers and crossed polarizers with a retardation plate. The HPC fibers induce tilted defect rings, shortening the yellow-colored parts and elongating the blue parts in the retardation plate image. (c,d) Streamlines of the director in the vertical cross section show how the nonzero angle of the surface anchoring breaks the symmetry between domains, which shrinks one type of domain and expands the other, tilting the rings. (e-f) The tilt of the rings is directly correlated to the angle of the surface anchoring angle α on the fibers (visualized as green ridges on top of the fiber). The fiber image is superimposed over a simulated lambda-plate transmission micrograph. On the bottom part, the micrograph is unobscured for easier comparison with (a,b).

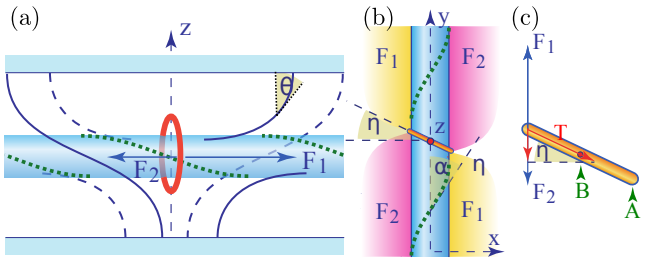

FIG. 4. (Color online) (a) A side-view of the director field geometry around the twisted fiber. The ring splits the fiber into two domains with oppositely oriented S-shaped director field streamlines (solid and dashed blue). The surface anchoring (dotted green) favors one of the orientations, and the resulting free energy difference pulls the ring sideways. (b) The top view sketch shows the arrangement of low (F_2) and high (F_1) free energy regions and the resulting tilt of the ring by the angle η. The angle α describes the helical surface alignment. (c) The force balance used to predict the tilting angle analytically. The difference of free energy per unit length of the fiber $F_{1,2}$, is balanced by the disclination line tension T.

first glimpsed in an experiment with nematic droplets on biofibers [27]. The ring normals are rotated in the imaging plane by a tilt angle with respect to the fiber axis. The magnitude of the tilt angle is consistent for all the rings on each individual fiber, independent on their separation, and strictly alternates in sign between adjacent rings. A fiber with the surface molecular alignment parallel to the fiber axis has a mirror symmetry and would produce a director with the same left-to-right symmetry. A chiral perturbation is needed to break the mirror symmetry and induce the observed tilting.

The HPC in its liquid crystalline form (before drying) exists in a cholesteric phase, so the polymer chains in the fiber exhibit a slight double-twist and run in a steep helix around the fiber [31]. As the anchoring chirality induces mechanical rotation – in this case the rotating objects are the disclination rings – we call this phenomenon *the chirogyral effect*. Numerical simulations show how the helical anchoring breaks the symmetry between adjacent domains (Fig. 3c,d) and reproduce the alternating tilting of disclination rings (Fig. 3e-f).

For a better understanding of the chirogyral effect, we compute an analytic estimate that relates the angle of the helical anchoring α to the angle η of the disclination ring tilt, defining the *chirogyral coefficient* η/α. While the elastic constant anisotropy plays a role in the optical micrograph, analytical computation calls for a simplified director field model with equal elastic constants ($K_1 = K_2 = K_3 = K$) so that the director lies in the yz plane, where θ is the angle between the director and the vertical (z) axis (see Fig. 4a).

The chirogyral effect arises from the difference in the elastic deformation on adjacent domains, separated by the disclination ring (Fig. 4b). On a vertical line (along the viewing direction) that just touches the fiber, the director rotates from vertical ($\theta = 0$) to the maximum deviation in the middle of the cell ($\theta = \frac{\pi}{2} \pm \alpha$), and then unwinds again. The director streamlines are thus S-shaped and gain a different slope in adjacent domains in the chiral case (Fig. 3c,d, Fig. 4). Far away from the fiber, we approach the far-field limit of undisturbed vertical director and the mid-cell θ decreases exponentially. On each side of the fiber, the free energy difference between adjacent domains exerts a longitudinal force with magnitude $F_1 - F_2$ on the disclination ring (Fig. 4b,c). This force is opposed by the line tension T, which equals the free energy cost of the disclination per unit length. The equilibrium ring tilt η is reached when the forces are in balance, $T \sin\eta = F_1 - F_2$ (Fig. 4c) [37].

The distortion free energy density, given by $f_{el} = \frac{1}{2}K(\nabla\theta)^2$, is minimized when $\theta(x, z)$ satisfies a Laplace equation. A solution compatible with the boundary conditions gives a linear proportionality of the free energy to the angle α (see Supplemental Material at [URL will be inserted by publisher], section I, for detailed derivation of the free energy). In the limit of small angles, the force balance gives an expression for the chirogyral coefficient,

$$\frac{\eta}{\alpha} \approx \frac{\pi^2}{2}\frac{K}{T}. \tag{3}$$

The effective disclination line tension T is the linear free energy density of the disclination and depends on the material constants and cell geometry. Due to the diverging elastic distortion at the defect core, the line tension is logarithmic in the ratio between the length scale of the core and the length scale of the bulk deformations [32]. The line tension generally varies along the ring due to differences in confinement and distortion geometry, so the ring is not necessarily planar. For a fiber of diameter d in a cell of thickness D an analytical calculation (see Supplemental Material at [URL will be inserted by publisher] for the derivation of the line tension) provides the chirogyral coefficient

$$\frac{\eta}{\alpha} \approx \frac{\pi}{\ln(D/4.57\xi)} \tag{4}$$

for the side part of the disclination (point A in Fig. 4c), and

$$\frac{\eta}{\alpha} \approx \frac{\pi}{\ln((D-d)/6.28\xi)}, \tag{5}$$

for the top part of the disclination, which feels the confinement by the cell walls (point B in Fig. 4c). The parameter ξ is the radius of the defect core, which is the scale of all the fine features between the defect and the fiber surface that were not taken into account explicitly (see Supplemental Material at [URL will be inserted by publisher], section II, for discussion about this parameter). It's worth noting that the chirogyral coefficient is independent of the elastic constants and the defect core radius ξ is the only length scale in the system.

If the fiber is not too confined, the extremal estimates of the chirogyral coefficient are similar and the disclination ring is planar. In very strongly confined cells, however, the top and bottom parts of the ring (point B in

Fig. 4c) has a steeper tilt angle compared to the side part (point A in Fig. 4c)

V. MECHANICALLY TWISTED FIBERS

Experiments with thin electrospun fibers are unsuitable for qualitative investigation of the tilting phenomenon, because the helical angle and the tilt angle can not be accurately measured. An experiment was performed with a thicker drawn-by-hand HPC fiber with diameter $d = 90\,\mu\text{m}$ in a cell with thickness $D \approx 100\,\mu\text{m}$ which was mechanically twisted, as shown in Fig. 5a,b. The cell has been filled with the eutectic commercial mixture EN18. Polarized micrographs revealed that without the mechanical twist, the disclination rings seem to be orthogonal to the fiber axis y within the accuracy of $\pm 1°$. This was expected, knowing that drawn-by-hand HPC fibers in EN18 are optically uniaxial because during the drawing process the HPC chains are stretched and aligned. Upon the mechanical twist, the orientation of chains on the fiber's surface becomes helicoidal. The tilt angle in Fig. 5b is $\eta = 18°$ and the scratches on the fiber surface help to determine the anchoring angle $\alpha = 15°$. This gives the chirogyral coefficient of $\eta/\alpha \approx 1.2$.

The same technique was used also on polyamide fibers (Nylon fishing lines) of diameter $d = 200\,\mu$m immersed in a variable thickness cell filled with the nematic 5CB. Linear dependence $\eta(\alpha)$ was measured for three cell thicknesses D, with the slopes measuring the chirogyral coefficient (Fig. 5c, see also Supplemental Video A at [URL will be inserted by publisher]). The effect of confinement ratio d/D on the tilt angle was measured and compared to the analytic prediction and numerical experiments, as witnessed in Fig. 5d, finding a good agreement (see also Supplemental Video B at [URL will be inserted by publisher]). In the extremely confined case, where the ring is practically touching the cell walls, the predicted S-shaped rings are also observed (Fig. 5e). Observe how the average tilt in this case differs from the steepest tilt, seen at the part of the ring closest to the cell walls and predicted by Eq. 5.

Figure 5c demonstrates the linear relationship between the tilt η and the helix angle α. Figure 5d shows the tilting angle dependence on the cell confinement and fiber diameter obtained by numerical simulation and experiments. Despite many approximations, the analytical description correctly reflects the dependency of the chirogyral coefficient on the cell and fiber thickness and can be used for quantitative prediction of the coefficient.

VI. CONCLUSION

We presented experimental results on observation of microfibers with planar nematic alignment on the surface, suspended in a homeotropic nematic cell. With electrospun CA and HPC fibers, we demonstrated the ability of using the chirogyral effect as means of recognizing the chiral fibers from the achiral ones. We reproduced the observed structures in simulation and explained how the elastic constant anisotropy reflects in the polarized transmission micrograph, which could be tuned to serve as a micro-probe for assessment of material properties.

The chirogyral effect that tilts the disclination ring under the influence of the fiber chirality was shown to be fundamentally geometric in origin, a direct consequence of chirality-induced symmetry breaking. The analytical predictions were quantitatively matched with experiments tailored to allow direct measurement of the chirogyral coefficient. With mechanical actuators to control the torsion of the fiber, the chirogyral effect was shown to be essentially a transmission from mechanical rotation to rotation of the defect ring and deformation director field around it. As such, it can be used as a possible building block in micromechanical and microfluidic devices. More generally, the presented approach offers a novel insight into mechanical manipulation of microfibers, imposing chirality into the fiber's surroundings.

ACKNOWLEDGMENTS

S.Č., D.S. M.R. and S.Ž. acknowledge funding from Slovenian research agency (ARRS), grant P1-0099. S.Č. also acknowledges ARRS grant Z1-6725, whereas M.R. the EU MC CIG grant FREEFLUID and USAF EOARD grant SOFTMETA. This work is also funded by FEDER through the COMPETE 2020 Program and National Funds through FCT-Portuguese Foundation for Science and Technology under projects UID/CTM/50025/2013 and PTDC/FIS/NAN/0117/2014. M.D. and P.P. would like to thank V. Klein, S. Saranga, J. Sanchez, J.-L. Signoret, M. Bottineau, V. Davouloury and A. Lecchi for technical support as well as P. Oswald, H. Kitzerow and I. Dozov for providing us with, respectively, SE-1211, EN18 and 5CB materials.

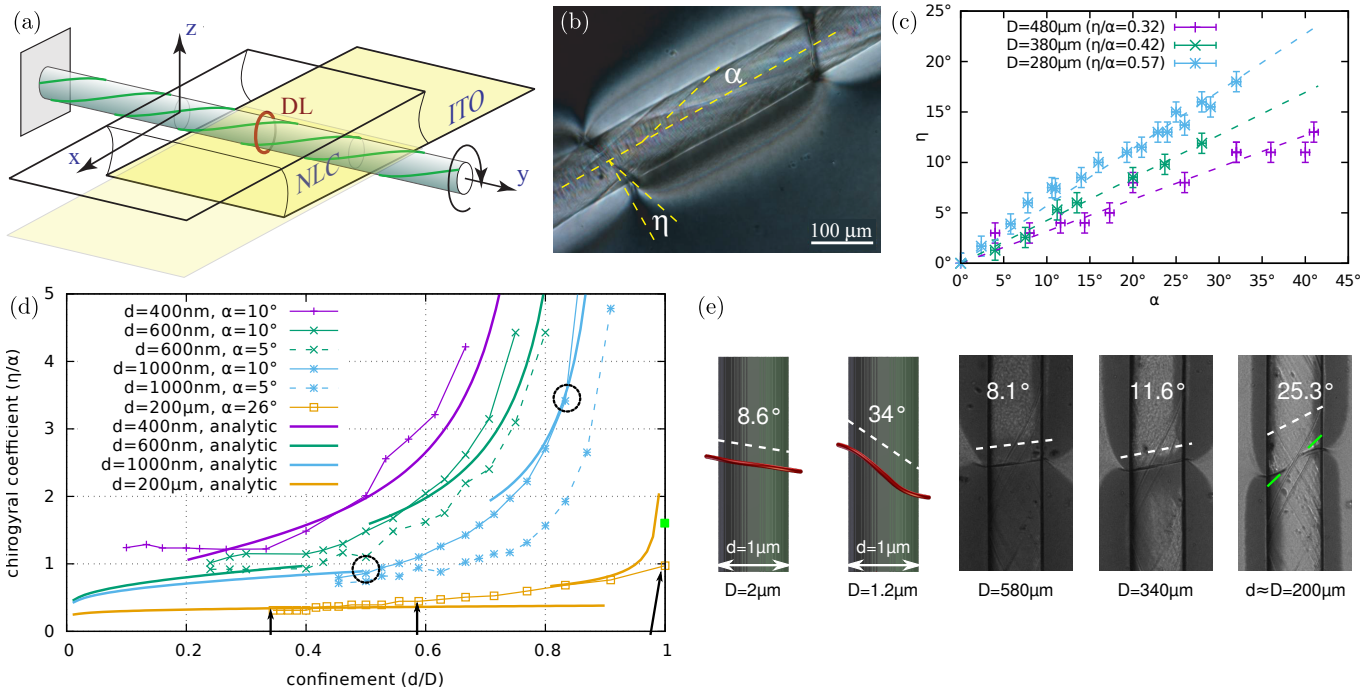

FIG. 5. (Color online) (a) A laboratory setup of the cell for mechanical twisting. The fiber is attached to stepping motors to control the twisting. An ITO layer treated with polyimide ensures homeotropic anchoring. (b) A micrograph of a 90 µm fiber hand-drawn from HPC. The helical angle α can be read out from the tilt in the surface scratches. The resulting tilt of the ring by the angle η is also visible. (c) Mechanically stepping the helical angle of a Nylon fiber at fixed cell thickness reveals the linear dependence of the tilt angle. The slope corresponds to the chirogyral coefficient. Fiber thickness is $d = 200\,\mu$m. (d) Comparison of the theoretically predicted chirogyral coefficient with experimental and numerical measurements, in relation to the confinement strength d/D and for different fiber thicknesses d. The analytic expressions obtained from the side line tension (Eq. 4, used for small d/D) and from the top line tension (Eq. 5, used for large d/D) are indicated. Experimental data was measured with 200 μm Nylon fibers. (e) Examples of disclination rings for weakly and strongly confined fibers in simulation (first two) and experiment (last three). The helical angle in simulation is $\alpha = 10^\circ$ and in experiment $\alpha = 26^\circ$. Strong confinement causes S-shaped rings, with the middle tilt (green) much steeper (as indicated by the green square in panel (d)). The circles in (d) mark the depicted simulated snapshots (first two panels in (e)), while the arrows mark the experimental micrographs.

[1] S. J. Woltman, G. D. Jay, and G. P. Crawford, Nat. Mater. **6**, 929 (2007).
[2] R. J. Carlton, J. T. Hunter, D. S. Miller, R. Abbasi, P. C. Mushenheim, L. N. Tan, and N. L. Abbott, Liquid Crystals Reviews **1**, 29 (2013).
[3] S. Sivakumar, K. L. Wark, J. K. Gupta, N. L. Abbott, and F. Caruso, Adv. Funct. Mater. **19**, 2260 (2009).
[4] U. Manna, Y. M. Zayas-Gonzalez, R. J. Carlton, F. Caruso, N. L. Abbott, and D. M. Lynn, Angew. Chem. Int. Ed. **52**, 14011 (2013).
[5] J. Kim, M. Khan, and S.-Y. Park, ACS Appl. Mater. Interfaces **5**, 13135 (2013).
[6] D. C. Zografopoulos, R. Asquini, E. E. Kriezis, A. d'Alessandro, and R. Beccherelli, Lab Chip **12**, 3598 (2012).
[7] J. G. Cuennet, A. E. Vasdekis, and D. Psaltis, Lab Chip **13**, 2721 (2013).
[8] U. Tkalec, M. Ravnik, S. Čopar, S. Žumer, and I. Muševič, Science **333**, 62 (2011).
[9] U. Tkalec and I. Muševič, Soft Matter **9**, 8140 (2013).
[10] B. Senyuk, Q. Liu, S. He, R. D. Kamien, R. B. Kusner, T. C. Lubensky, and I. I. Smalyukh, Nature **493**, 200 (2013).
[11] A. Martinez, M. Ravnik, B. Lucero, R. Visvanathan, S. Žumer, and I. I. Smalyukh, Nat. Mater. **13**, 258 (2014).
[12] G. P. Alexander, B. G. ge Chen, E. A. Matsumoto, and R. D. Kamien, Rev. Mod. Phys. **84**, 497 (2012).
[13] S. Čopar, Phys. Rep. **538**, 1 (2014).
[14] I. Muševič, M. Škarabot, and M. Humar, J. Phys.: Condens. Matter **23**, 284112 (2011).
[15] M. Humar and I. Muševič, Opt. Express **18**, 26995 (2010).
[16] T. Kosa, L. Sukhomlinova, L. Su, B. Taheri, T. J. White, and T. J. Bunning, Nature **485**, 347 (2012).
[17] A. Sengupta, S. Herminghaus, and C. Bahr, Liquid Crystals Reviews **2**, 73 (2014).
[18] T. Araki, M. Buscaglia, T. Bellini, and H. Tanaka, Nat. Mater. **10**, 303 (2011).
[19] O. D. Lavrentovich, Proc. Natl. Acad. Sci. **108**, 5143 (2011).
[20] I. C. Khoo, Progress in Quantum Electronics **38**, 77 (2014).
[21] Q. Zhao, L. Kang, B. Du, B. Li, J. Zhou, H. Tang, X. Liang, and B. Zhang, Appl. Phys. Lett. **90**, 011112 (2007).
[22] U. Tkalec, M. Škarabot, and I. Muševič, Soft Matter **4**, 2402 (2008).
[23] D. A. Beller, M. A. Gharbi, and I. B. Liu, Soft Matter **11**, 1078 (2015).
[24] A. Golovin, J. Xiang, H.-S. Park, L. Tortora, Y. Nastishin, S. Shiyanovskii, and O. Lavrentovich, Materials **4**, 390 (2011).
[25] Q. Liu, B. Senyuk, J. Tang, T. Lee, J. Qian, S. He, and I. I. Smalyukh, Phys. Rev. Lett. **109**, 088301 (2012).
[26] M. Nikkhou, M. Škarabot, S. Čopar, M. Ravnik, S. Žumer, and I. Muševič, Nature Phys. **11**, 183 (2015).
[27] L. E. Aguirre, A. de Oliveira, D. Seč, S. Čopar, P. L. Almeida, M. Ravnik, M. H. Godinho, and S. Žumer, to appear in PNAS.
[28] V. S. R. Jampani, M. Humar, and I. Muševič, Opt. Express **21**, 20506 (2013).
[29] Y. Geng, D. Seč, P. L. Almeida, O. D. Lavrentovich, S. Žumer, and M. H. Godinho, Soft Matter **9**, 7928 (2013).
[30] Y. Geng, P. L. Almeida, J. L. Figueirinhas, E. M. Terentjev, and M. H. Godinho, Soft Matter **8**, 3634 (2012).
[31] J. P. Canejo, J. P. Borges, M. H. Godinho, P. Brogueira, P. I. C. Teixeira, and E. M. Terentjev, Adv. Mater. **20**, 4821 (2008).
[32] P. G. de Gennes and J. Prost, *The Physics of Liquid Crystals* (Oxford Science Publications, Oxford, ed. 2, 1993).
[33] D. Seč, T. Lopez-Leon, M. Nobili, C. Blanc, A. Fernandez-Nieves, M. Ravnik, and S. Žumer, Phys. Rev. E **86**, 020705 (2012).
[34] M. Ravnik, M. Škarabot, S. Žumer, U. Tkalec, I. Poberaj, D. Babič, N. Osterman, and I. Muševič, Phys. Rev. Lett. **99**, 247801 (2007).
[35] M. Ravnik and S. Žumer, Liq. Cryst. **36**, 1201 (2009).
[36] A. Nych, U. Ognysta, I. Muševič, D. Seč, M. Ravnik, and S. Žumer, Phys. Rev. E **89**, 062502 (2014).
[37] M. Stephen and J. Straley, Rev. Mod. Phys. **46**, 617 (1974).